Crystallographic ordering in a series of Al-containing refractory high entropy alloys Ta-Nb-Mo-Cr-Ti-Al

*H. Chen[a], A. Kauffmann[a], S. Seils[ab], T. Boll[ab], C. H. Liebscher[c], I. Harding[d], K. S. Kumar[d], D. V. Szabó[ab], S. Schlabach[ab], S. Kauffmann-Weiss[e], F. Müller[f], B. Gorr[f], H.-J. Christ[f], and M. Heilmaier[a]**

[a] Institute for Applied Materials (IAM-WK), Karlsruhe Institute of Technology (KIT), Engelbert-Arnold-Str. 4, 76131 Karlsruhe, Germany

[b] Karlsruhe Nano Micro Facility (KNMF), Karlsruhe Institute of Technology (KIT), Hermann-von-Helmholtz-Platz 1, 76344 Eggenstein-Leopoldshafen, Germany

[c] Max-Planck-Institut für Eisenforschung GmbH, Max-Planck-Straße 1, 40237 Düsseldorf， Germany

[d] School of Engineering, Brown University, Providence, Rhode Island 02912, USA

[e] Institute for Technical Physics (ITEP), Karlsruhe Institute of Technology (KIT), Hermann-von-Helmholtz-Platz 1, 76344 Eggenstein-Leopoldshafen, Germany

[f] Institut für Werkstofftechnik, Universität Siegen, Paul-Bonatz-Str. 9-11, 57068 Siegen, Germany

**corresponding author*
mail: martin.heilmaier@kit.edu, phone: +4972160846594

Abstract

High entropy alloys based on the Ta-Nb-Mo-Cr-Ti-Al system are expected to possess high creep and oxidation resistance as well as outstanding specific mechanical properties due to presumed high melting points and low densities. However, we recently reported that arc-melted and subsequently homogenized alloys within this system exhibit a lack of ductility up to 600 °C [H. Chen et al. in Metall. Mater. Trans. A 49 (2018) 772-781 and J. Alloys Cmpd. 661 (2016) 206-215]. Thermodynamic calculations suggest the formation of a B2-type ordered phase below the homogenization temperature. In the present article, we provide results of a detailed microstructural characterization of a series of Ta-Nb-Mo-Cr-Ti-Al derivatives and evaluate if B2-type ordering could be the origin for the observed lack of ductility. Backscatter electron (BSE) imaging, energy dispersive X-ray spectroscopy (EDX) and atom probe tomography (APT) were used to verify uniform elemental distribution after homogenization. X-ray diffraction (XRD) patterns indicate both, A2 or B2-type crystal structure, whereas transmission electron microscopy (TEM) diffraction experiments unambiguously confirmed B2-type order in the as-homogenized state of all investigated alloys. In MoCrTiAl, planar defects that show antiphase boundary contrast with a {100}-type habit plane were detected by TEM dark field (DF) imaging. They are wetted by a Cr-enriched and Ti-depleted layer as confirmed by scanning transmission electron microscopy (STEM)-EDX line scans as well as APT analyses. The planar defects arise from a disorder-order solid-state phase transformation during cooling, as indicated by differential scanning calorimetry (DSC).

Keywords

high entropy alloys; ordering; thermal antiphase domain boundaries; phase transition; segregation.

1. Introduction

The term high entropy alloys (HEAs) was introduced by Yeh et al. [1]. They suggested the development of equiatomic, multi-principal element alloys that are expected to exhibit single-phase solid solutions with simple crystal structures due to the maximization of the configurational entropy contribution to Gibb's free energy. This concept promotes a huge variability in alloy design due to the flexibility in selecting and combining elements that may fulfill the respective requirements compared to conventional alloys, which are usually based on a single principal element. Already, a large number of new structural materials with outstanding mechanical properties was found, summarized in a recent review by Gorsse et al. [2]. Consequently, the potential of this alloying strategy for high temperature materials was immediately recognized through the development of high entropy alloys containing refractory metals [3] which have recently been summarized by Senkov et al. [4].

Starting from 2016, we have presented several Al-containing refractory HEA (RHEA) derivatives from the Ta-Nb-Mo-Cr-Ti-Al system which were produced by arc melting and subsequent homogenization and furnace cooling [5–7]. XRD suggests an A2-type crystal structure (W prototype) after homogenization. Although being tested in mostly single-phase condition, the Ta-Nb-Mo-Cr-Ti-Al system has not shown significant macroscopic plastic deformation at temperatures below 600 °C in terms of compression tests. The reasons for this rather brittle behavior have been discussed, yet not clarified [5,6]. We previously assumed that Kirkendall porosity or compatibility stresses due to grain growth during homogenization lead to inhomogeneous stress distribution within the compression samples and, therefore, favor crack initiation and propagation.

Similar observations are found in literature for other single-phase RHEAs [8–12]. As an example, NbMoTaW exhibits poor plastic, compressive deformation behavior at room temperature of about 2 % plastic strain to failure. Although XRD patterns suggest a disordered bcc crystal structure (W prototype, Strukturbericht A2), Widom et al. [13] and Körmann et al. [14] calculated that crystallographic order of B2-type might be present in NbMoTaW at room temperature. Similarly, the crystal structure of homogenized AlNbTiV was firstly stated to be of A2-type crystal structure since the corresponding XRD pattern did not exhibit superstructure peaks [15]. The crystal structure was later revised to be of B2-type; however, the missing superstructure peaks in the XRD patterns were not discussed [16]. The same publication revealed the presence of thermal antiphase domain boundaries (APDBs) in AlNbTiV, but did not characterize these microstructural features in detail. Also, the temperature at which the APDBs form has not been investigated. In summary, single-phase B2-type ordered crystal structures have been suggested. Nevertheless, these were either not experimentally proven or not discussed in detail. It is assumed that crystallographic order might be a crucial point for RHEAs to exhibit brittle behavior under mechanical load at low temperatures. Hence, we present investigations on ordering in alloys from the Ta-Nb-Mo-Cr-Ti-Al system and discuss the peculiarities of ordering in multicomponent systems using a combination of advanced characterization techniques.

Thermodynamic calculations of Ta-Nb-Mo-Cr-Ti-Al derivatives reveal that a B2-type ordered phase can form during furnace cooling subsequent to homogenization. Therefore, chemical homogeneity is profoundly proven first and verified across different length scales using back scatter electron imaging in the scanning electron microscope (SEM-BSE), energy dispersive X-ray spectroscopy (SEM-EDX) being complemented by APT. XRD and TEM-SAD are used to characterize the crystal structure. (S)TEM experiments reveal planar lattice defects that possess a {100}-type habit plane and that are wetted by a Cr-enriched and Ti-depleted segregation layer.

2. Methods

To reveal if ordering might occur in Ta-Nb-Mo-Cr-Ti-Al, thermodynamic calculations were carried out using the software FactSage V7.2 in conjunction with a commercial database, which includes all elements constituting the presented alloys. Step size of temperature for calculations was 10 K.

The investigated alloys were manufactured by arc melting. The elements Ta, Nb, Mo, Cr, Ti and Al with their respective nominal purities of 99.9, 99.9, 99.96, 99, 99.8 and 99.9 % were mixed in the required compositions and placed in the vacuum chamber of an AM/0.5 arc melting furnace by Edmund Bühler GmbH (Germany). The furnace chamber was alternately pumped down to a pressure of $5 \cdot 10^{-2}$ mbar and flooded with Ar up to ambient pressure for three times. A high vacuum environment at $1 \cdot 10^{-4}$ mbar was subsequently established. The working Ar pressure for the melting operation was 600 mbar. The manufactured ingots were flipped, remelted for at least five times and cast into a water-cooled, rod-shaped Cu mold with a diameter of 12 mm and a length of 60 mm. Using a HTRH tube furnace by Carbolite Gero GmbH & Co. KG (Germany), a homogenization treatment was employed at 1200 °C (MoCrTiAl), 1300 °C (NbMoCrTiAl) and 1500 °C (NbMoTiAl and TaMoCrTiAl) for 20 h, respectively, depending on the alloy composition. For this purpose, an Ar atmosphere was established within the furnace tube. The heating and cooling rate were 250 K/h each. The chemical composition of the investigated alloys is presented in Tab. 1. Maximum deviation for individual elements from the nominal composition is 1.0 at.%. The compositions of MoCrTiAl, NbMoTiAl and TaMoCrTiAl were determined by ICP-OES whereas the composition of NbMoCrTiAl was analyzed by standard-related EDX which coincides well with the ICP-OES technique.

Table 1: Chemical compositions $\bar{x}_i$ of the investigated alloys in at.%; * denotes ICP-OES, † indicates standard-related EDX.

alloy	heat treatment condition	$\bar{x}_i$ / at.%					
		Ta	Nb	Mo	Cr	Ti	Al
MoCrTiAl*	1200 °C / 20 h	–	–	24.8	24.9	24.9	25.4
NbMoCrTiAl†	1300 °C / 20 h	–	21.0	20.5	19.1	20.1	19.3
NbMoTiAl*	1500 °C / 20 h	–	25.5	25.3	–	24.9	24.3
TaMoCrTiAl*	1500 °C / 20 h	20.1	–	19.5	19.8	20.4	20.2

SEM-BSE imaging and SEM-EDX were performed on round-shaped discs, which were cut from the homogenized rods. The discs were prepared using a combined mechanical and chemical preparation procedure utilizing grinding, subsequent polishing and etching in NH_3, H_2O_2 and distilled water in a ratio of 1 : 2 : 7 at 30 °C for 5 min. For SEM analysis, we used an Auriga dual beam scanning electron

and focused ion beam (FIB) microscope by Carl Zeiss AG (Germany) equipped with an EDAX Octane silicon drift detector EDX system at 25 kV. Crystallographic investigations were carried out on a Bruker D8 Discover XRD device equipped with a 1D LynxEye Xe detector. Scans were carried out with a step size of 0.01° in 2Θ at a scan time of acquisition time of 576 s per step while rotating the sample. The samples for XRD were crushed in an agate mortar, embedded in resin and finally metallographically prepared in order to increase peak intensity.

For (S)TEM investigations, platelets with diameters of 3 mm were cut by electrical discharge machining and ground down to a thickness of 100 µm. Finally, the specimens were jet-polished with a TenuPol-5 by Struers GmbH at room temperature, using a voltage of 12 V and an electrolyte consisting of H_2SO_4 and methanol in a ratio of 1 : 4 . TEM bright field (TEM-BF) imaging and TEM-SAD were carried out on a CM20 by FEI-Philips, a JEM-2100 by JEOL, a Tecnai F20ST and an image corrected Titan Themis 80-300 by FEI. All microscopes were operated at an accelerating voltage of 200 kV or 300 kV, respectively. STEM datasets were acquired in a monochromated, C_s probe-corrected Titan Themis 60-300 (FEI Thermo Fisher Scientific) equipped with a four quadrant ChemiSTEM EDS system operated at an acceleration voltage of 300 kV. For HAADF imaging a semi-convergence angle of 17 mrad, probe current of 80 pA and collection angles of the annular detector of 73 mrad to 200 mrad were utilized. A serial acquisition scheme of 20 to 30 images at a pixel dwell time of 2 µs was employed to reduce the influence of scan noise. The final image is obtained by cross-correlation and averaging. The probe current was increased to 150 up to 250 pA for high resolution STEM-EDX elemental mapping.

A Strata dual beam SEM/FIB device by FEI (Netherlands) was used to manufacture tips for APT. The tips were taken from several grains. The regions to be prepared for analysis were first protected by the deposition of Pt to avoid damage from the Ga^+ beam. An originally (30 x 4 x 3) μm^3 sized rod was cut from the material and parts of it were transferred to a coupon with pre-sharpened Si micro-posts provided by Cameca SAS (France). Annular milling at 30 kV acceleration voltage with decreasing inner diameter down to 0.2 µm and decreasing beam current, was conducted to obtain tip shaped specimens. Final milling with a closed circular pattern was performed at 5 kV acceleration voltage to minimize the Ga^+ affected layer at the surface. A LEAP 4000X HR atom probe by Cameca SAS was used in pulsed voltage mode for the analyses. Voltage pulses had a repetition rate of 200 kHz with a fraction of 20 % of the standing voltage. Standing voltage was controlled automatically to ensure a detection rate of 1 % (= fraction of pulses, leading to the detection of an ion). All reconstructions and analyses of tips shown in this paper were conducted with the IVAS 3.6.14 software of Cameca SAS.

Dynamic DSC experiments were carried out on a 404 F1 Pegasus by Netzsch-Gerätebau GmbH (Germany). The derivative of enthalpy with respect to temperature dH/dT was determined by

comparison with a sapphire crystal (provided by Netzsch-Gerätebau GmbH) including drift correction as presented in the DIN 51007 standard.

3. Results and discussion

3.1 Chemical homogeneity

An almost single-phase microstructure is observed in the BSE micrographs of Fig. 1 for equiatomic MoCrTiAl, NbMoCrTiAl, NbMoTiAl and TaMoCrTiAl after suitable homogenization treatments. We were able to suppress most of the secondary phases to below a limit of 0.3 vol.% in all investigated alloys. Most of these secondary, intermetallic phases were characterized by combined EDX, XRD and EBSD analysis [5,6]. Additionally, we found traces of the hexagonal Laves phase $TaCr_2$ ($MgZn_2$ prototype, Strukturbericht designation C14) at the grain boundaries of as-homogenized TaMoCrTiAl which are highlighted by black arrows in Fig. 1d. The EDX maps of the alloying elements show almost uniform element distribution within the analyzed regions whereas the oxygen map does not indicate any formation of oxides.

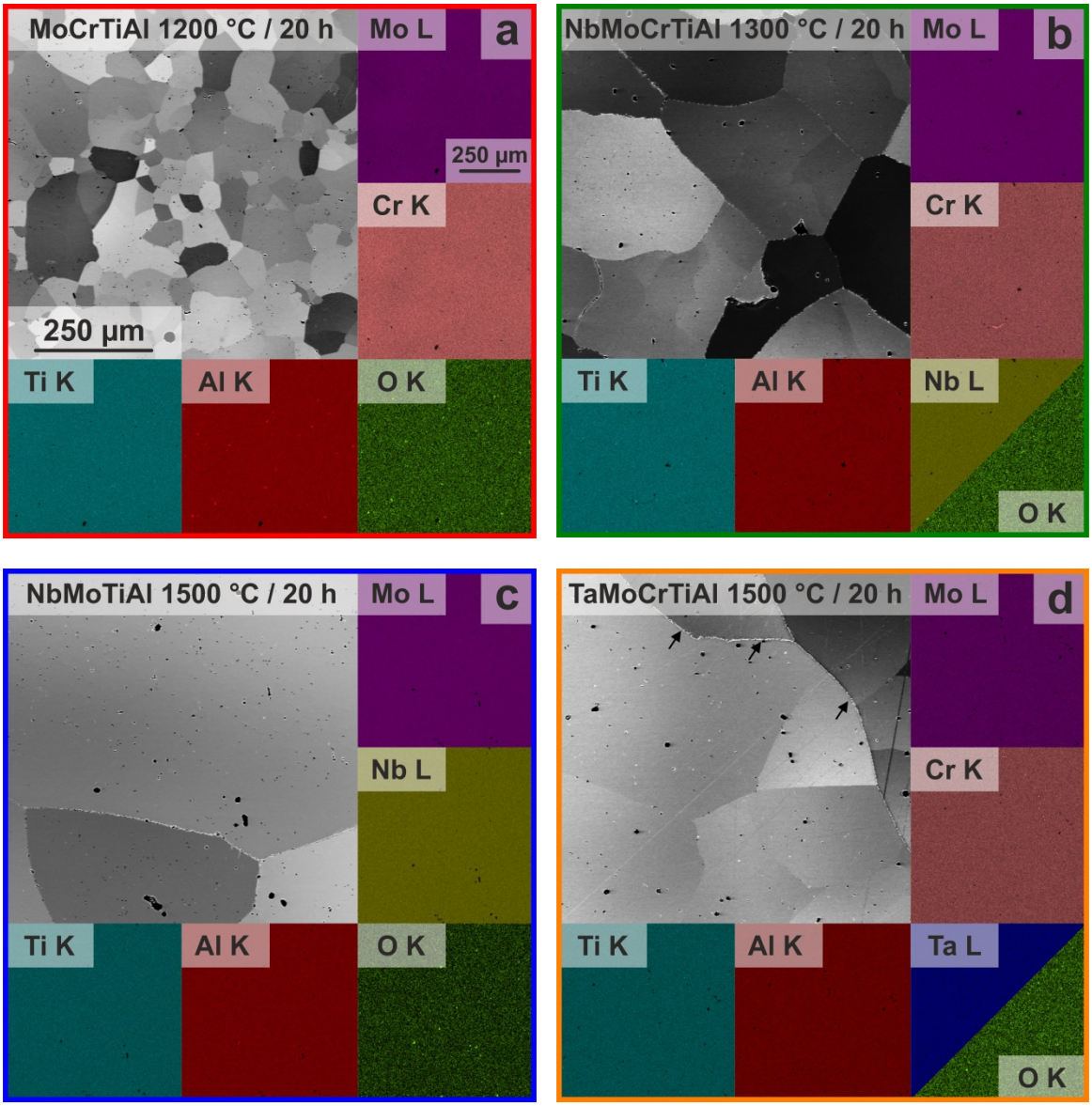

Figure 1: SEM-BSE images (upper left corner) and corresponding EDX maps (insets) of the same field of view of all investigated alloys: a) MoCrTiAl, b) NbMoCrTiAl, c) NbMoTiAl, and d) TaMoCrTiAl. All BSE micrographs and EDX maps are taken at the same magnification.

To verify chemical homogeneity on a nanometer length scale, we performed APT on three alloys (MoCrTiAl, NbMoTiAl, and TaMoCrTiAl). Fig. 2a presents a comparison of the mean element concentrations $\bar{x}_i$ of several APT tips of MoCrTiAl. The APT tips no. "I" to "IV" are taken from one and the same grain whereas APT tip no. "V" is taken from an adjacent grain. There is no indication of segregation on the investigated distance of approx. 20 µm within the one grain as well as in the adjacent one. Similar results with the absence of segregation were found in the other two alloys, namely NbMoTiAl and TaMoCrTiAl (not shown here). Maximum difference of mean concentrations of the elements $\bar{x}_i$ between two different tips was 0.4 at.%. The ion distributions within all analyzed APT tips were investigated as well. As an example, the elemental distributions from APT tip no. "IV" of MoCrTiAl are presented in Fig. 2b for an evaluation using N bins of $n_b = 100$ ions in size along a

cylindrical volume as highlighted in Fig. 2c. The obtained distributions of the elements i are binomial-like:

$$f_i(n) = N \cdot \frac{n_b!}{n! \cdot (n_b - n)!} \cdot \bar{x}_i^n \cdot (1 - \bar{x}_i)^{n_b - n}. \quad (1)$$

The normalized mean quadratic deviation of the experimentally observed distribution $e_i(n)$ from the binomial one is as follows:

$$\chi_i^2 = \sum_{n=0}^{n_b} \frac{\left(e_i(n) - f_i(n)\right)^2}{f_i(n)}. \quad (2)$$

It was calculated to determine a sample volume independent auto-correlation factor:

$$\mu_i = \sqrt{\frac{\chi_i^2}{N + \chi_i^2}}. \quad (3)$$

This parameter was introduced in Ref. [17] and is presented in Tab. 2. The obtained μ_i values are close to zero and, therefore, represent chemical homogeneity. For example, μ_i determined from APT analyses on non-equiatomic $Fe_{40}Mn_{27}Ni_{26}Co_5Cr_2$ (at.%) by Yao et al. [18] were in a comparable range, namely between 0.0078 and 0.0735. They concluded the solid solution to be random [18].

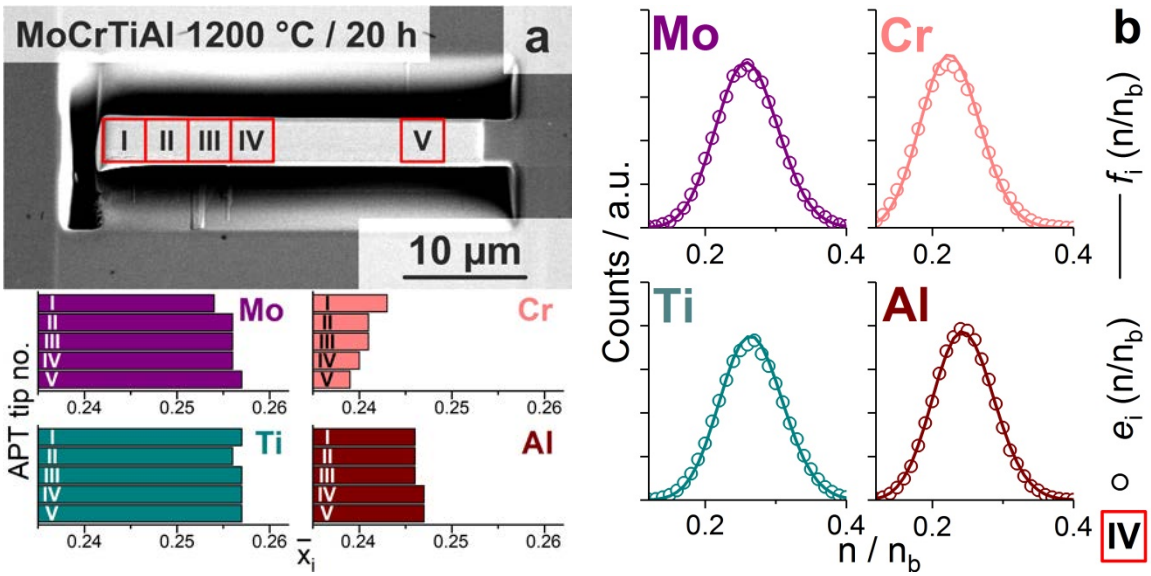

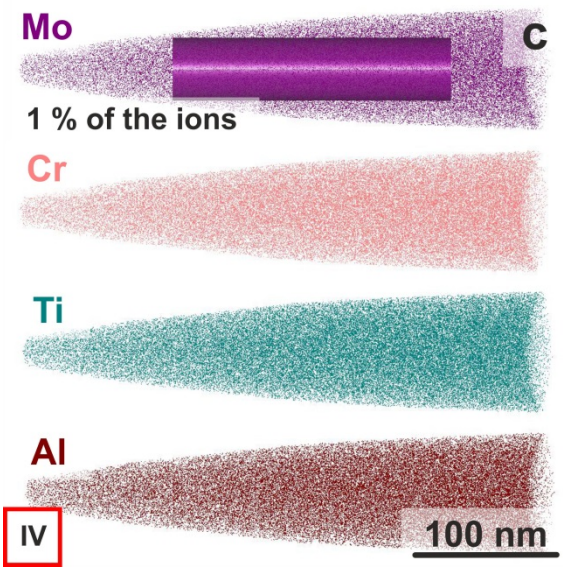

Figure 2: Summary of APT results on MoCrTiAl: a) locations of the investigated APT tips in an SEM image and the total composition of the tips, b) distribution of element concentrations in a cylindrical sample volume in tip no. "IV" highlighted in violet color in the corresponding ion maps of c) of the same APT tip. Color coding of the elements is identical to Fig. 1.

Table 2: Sample volume independent correlation factor μ_i describing the element distribution within the APT tips "I" – "V" of MoCrTiAl.

i	Mo	Cr	Ti	Al
μ_i / 10^{-2}	5.48 ± 1.30	9.26 ± 1.31	5.49 ± 0.43	3.37 ± 0.99

3.2 Appearance of order and microstructural peculiarities

Fig. 3 presents the temperature-dependent equilibrium phase distribution of equiatomic MoCrTiAl as predicted by FactSage. The alloy exhibits single-phase with an A2-type crystal structure (W prototype) above 1110 °C and in particular at the homogenization temperature of 1200 °C (highlighted by triangular symbols in Fig. 3. Below 850 °C, an A15-type phase (Cr_3Si prototype, square symbols in Fig. 3) is present in comparably low phase fraction. The A15-type phase was not found in the as-homogenized state by SEM. It is, thus, suggested that the cooling rate is sufficiently high to suppress the A15-type phase formation during furnace cooling. Between 1100 and 1110 °C, A2-type solid solution is predicted to completely transform into a B2-type phase (CsCl prototype, cross symbols in Fig. 3) during cooling. Thermodynamic calculations with an appropriate database therefore indicate an ordering transformation (A2 to B2-type crystal structure) during furnace cooling which could also occur in other derivatives of the Ta-Nb-Mo-Cr-Ti-Al system.

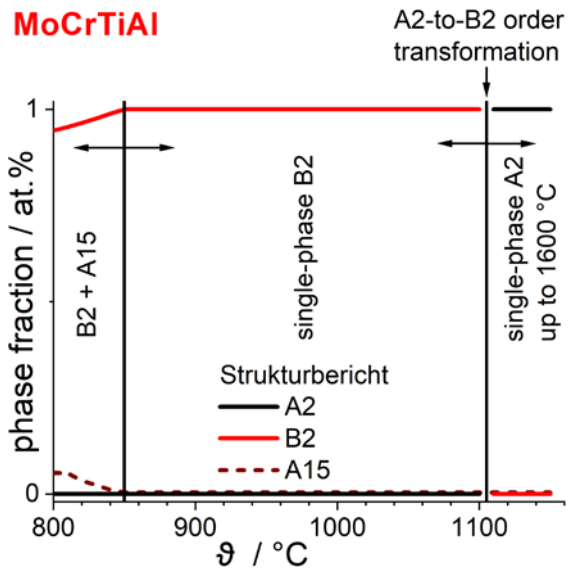

Figure 3: Temperature-dependent equilibrium phase distribution of equiatomic MoCrTiAl in the temperature range of 800 °C up to 1150 °C as-calculated by FactSage; step size of calculations was 10 K. Solidus temperature and liquidus temperature are calculated to be 1600 °C and 1800 °C, respectively (not shown here).

The presence of an ordered crystal structure after homogenization and furnace cooling was investigated by powder XRD of MoCrTiAl, NbMoCrTiAl, NbMoTiAl and TaMoCrTiAl (see XRD patterns in Fig. 4a). They reveal peaks that can be assigned to an A2-type (W prototype, closed diamonds) crystal structure. In addition, there are gentle indications of a B2-type crystal structure (CsCl prototype, half-closed diamonds) in NbMoCrTiAl and NbMoTiAl. These two alloys exhibit {100} superlattice peaks with intensities $I_{\{100\}}$ that remain small compared to the corresponding {200} peak intensities $I_{\{200\}}$, namely $\frac{I_{\{100\}}}{I_{\{200\}}} < 10.0\,\%$. For better visibility, the {100}-superlattice peak and corresponding {200}-fundamental peak of NbMoCrTiAl are highlighted in Fig. 4b. Further possible B2-superlattice peaks ($\{111\}$, $\{210\}$, etc. as indicated by open diamonds) cannot be found in these two alloys. The Nb-free derivative MoCrTiAl does not show any indications for order as per XRD. In contrast, B2-type order in TaMoCrTiAl is unambiguously observed in the XRD pattern by the appearance of all expected superlattice peaks. The {100}-superlattice peak shows an intensity comparable to that of the {200} peak: $\frac{I_{\{100\}}}{I_{\{200\}}} = 62.9\,\%$. Apart from the already assigned peaks, no further indications of secondary phases were observed in all cases supporting statement above that their respective volume fractions are small compared to the major A2/B2-type phase.

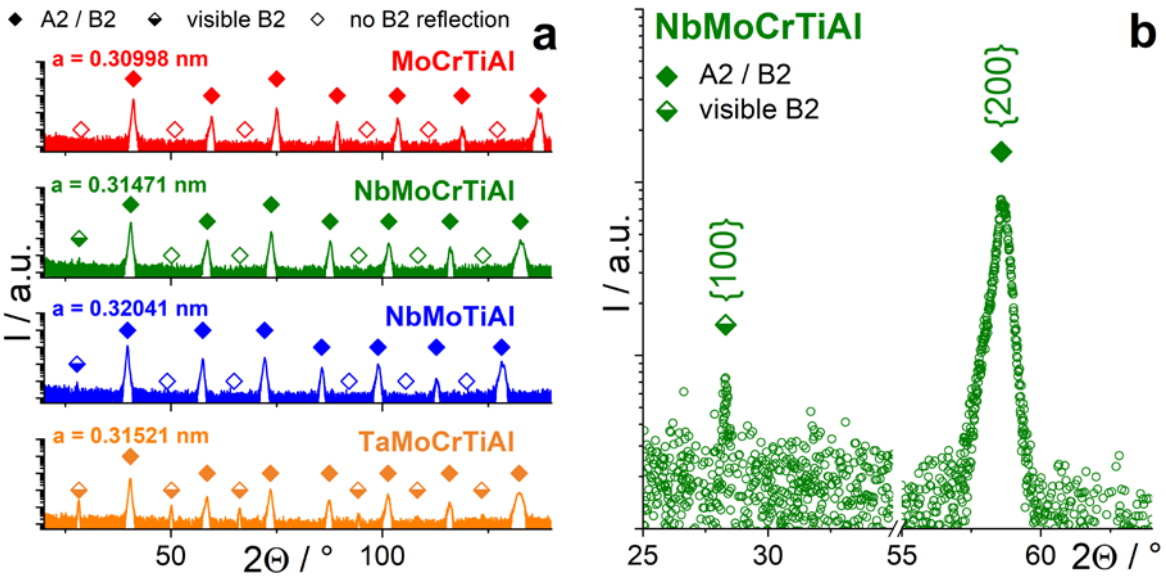

Figure 4: a) XRD patterns of all presented alloys. Intensity is plotted on a logarithmic scale for better visibility of low-intensity peaks. Closed diamonds indicate A2 peaks, half-closed diamonds show visible B2 superlattice reflections. B2 superlattice reflections were not observed at Bragg angles with open diamonds; b) XRD pattern of NbMoCrTiAl in a 2Θ-range of 25° up to 35° and 55° up to 65°, respectively, for better visibility of the {100} superlattice peak and the {200} fundamental peak. Color code is identical to Fig. 1.

In conclusion, NbMoCrTiAl, NbMoTiAl and TaMoCrTiAl exhibit at least one superlattice peak (namely {100}), indicating a B2-type ordered crystal structure. In contrast, not even the {100} peak is visible in MoCrTiAl against the background level of XRD. Whether missing superstructure peaks in the XRD pattern of MoCrTiAl (Fig. 4, top) may be a definitive proof for the absence of order will be discussed next. The intensity ratio of the {100}- and {200}-peaks $\frac{I_{\{100\}}}{I_{\{200\}}}$ depends on the site occupation factors SOF_i^{LS} of the elements i on the crystal lattice sites LS. In B2-type ordered, equiatomic MoCrTiAl, the four present elements would occupy two distinct lattice sites ($LS = 1$ for Wyckoff position "1a" and $LS = 2$ for Wyckoff position "1b"). Table 3 presents the structure factors $|F_{\{100\}}|$, $|F_{\{200\}}|$, and the ratio $\frac{|F_{\{100\}}|}{|F_{\{200\}}|}$ for different possible element configurations of completely B2-type ordered MoCrTiAl (highlighted by "♦" in Tab. 3). The maximum $\frac{|F_{\{100\}}|}{|F_{\{200\}}|} = 44.8\ \%$ is obtained for the B2 configuration with (Mo,Cr) on $LS = 1$ and (Ti,Al) on $LS = 2$ under the constraint of equiatomic composition. In comparison, $\frac{|F_{\{100\}}|}{|F_{\{200\}}|}$ is only $13.2\ \%$ for (Mo,Al) on $LS = 1$ and (Cr,Ti) on $LS = 2$, although both configurations have the same extent of B2-type order, namely two pairs of the constituting elements are in each case entirely distributed on a single lattice site. This situation might be called maximum extent of order for a quaternary, equiatomic alloy in a crystal structure with two distinct lattice sites.

Consequently, $\frac{|F_{\{100\}}|}{|F_{\{200\}}|}$ and, therefore, $\frac{I_{\{100\}}}{I_{\{200\}}}$ strongly depend on the combination of SOF_i^{LS} on the respective lattice sites. So far, only B2-type crystal structure configurations with maximum extent of order ($SOF_i^{LS} = 0$ or 0.5) have been considered. When SOF_i^{LS} approaches the mean site occupancy factors for equiatomic, four-component alloys of $\overline{SOF} = 0.25$, $\frac{|F_{\{100\}}|}{|F_{\{200\}}|}$ decreases correspondingly as it is presented for the partially ordered B2-type configuration "#" in Tab. 3. If we assume that $\frac{|F_{\{100\}}|}{|F_{\{200\}}|}$ and, therefore, $\frac{I_{\{100\}}}{I_{\{200\}}}$ continuously decrease to an extent that $I_{\{100\}}$ vanishes into the background of the XRD pattern, partial order of MoCrTiAl is still conceivable although a corresponding superstructure peak is not visible.

Table 3: Structure factors $|F_{\{hkl\}}|$ for various crystallographic configurations and the according site occupation factors SOF_i^{LS} for equiatomic MoCrTiAl considering two distinct lattice sites LS occupied by elements i; maximally ordered (♦), partially ordered (#) and disordered (+) configurations are presented; elements of B2 configurations that predominantly occupy one respective lattice site are written in italics.

	configuration	$\boldsymbol{SOF_i^1}$ $\boldsymbol{LS = 1}$				$\boldsymbol{SOF_i^2}$ $\boldsymbol{LS = 2}$				$\boldsymbol{\lvert F_{\{100\}}\rvert}$	$\boldsymbol{\lvert F_{\{200\}}\rvert}$	$\boldsymbol{\frac{\lvert F_{\{100\}}\rvert}{\lvert F_{\{200\}}\rvert}}$ **/ %**
		Mo	Cr	Ti	Al	Mo	Cr	Ti	Al			
♦	**(*Mo*,*Cr*)(*Ti*,*Al*)**	0.5	0.5	0	0	0	0	0.5	0.5	13.89	30.99	44.8
♦	**(*Mo*,*Ti*)(*Cr*,*Al*)**	0.5	0	0.5	0	0	0.5	0	0.5	11.53	30.99	37.2
♦	**(*Mo*,*Al*)(*Cr*,*Ti*)**	0.5	0	0	0.5	0	0.5	0.5	0	4.10	30.99	13.2
#	**(*Mo*,Cr,Ti,*Al*)(Mo,*Cr*,*Ti*,Al)**	0.375	0.125	0.125	0.375	0.125	0.375	0.375	0.125	2.05	30.99	6.6
+	**(Mo,Cr,Ti,Al)(Mo,Cr,Ti,Al)**	0.25	0.25	0.25	0.25	0.25	0.25	0.25	0.25	0	30.99	0

As discussed explicitly for MoCrTiAl, XRD is not capable to identify a potential B2-type crystal structure by clearly indicating superlattice peaks. Other diffraction techniques might be able to detect superlattice reflections of a B2-type ordered phase in MoCrTiAl. Hence, TEM experiments were carried out and are presented in the following. Fig. 5 presents TEM-BF and -SAD investigations on TaMoCrTiAl as reference alloy for the presence of superlattice reflections (as seen in the XRD pattern of Fig. 4) as well as MoCrTiAl. The BF images of both alloys (Fig. 5a & c) confirm the presence of single-phase microstructures in agreement with the previous investigations by SEM-BSE (Fig. 1a & d), SEM-EDX (Fig. 1a & d), APT (Fig. 2a & c) and XRD (Fig. 4) although some spots with darker contrast in the BF image of TaMoCrTiAl were found. However, they are not expected to be precipitates since APT did not provide evidence for them. At the current state of research, they are rather supposed to be artifacts

induced by electrolytic sample preparation. In addition, planar defects are visible in both cases (highlighted by arrows in Fig. 5a and c). Yurchenko et al. [16] found similar features in AlNbTiV and $AlNbTiVZr_{0.5}$ and referred to them as thermal APDBs. In MoCrTiAl, the planar defects seem to have distinct crystallographic orientations. They were not found in the NbMoTiAl microstructure. While there were no indications for order by XRD in the case of MoCrTiAl (see Fig. 4, top), TEM-SAD provides unambiguous evidence for ordering in both presented alloys (Fig. 5b & d). The corresponding $\{100\}$ and $\{111\}$ superlattice spots are marked in Fig. 5b & d. Order was also observed in NbMoCrTiAl and NbMoTiAl by gentle indications of superlattice spots in the respective SAD patterns (not shown here).

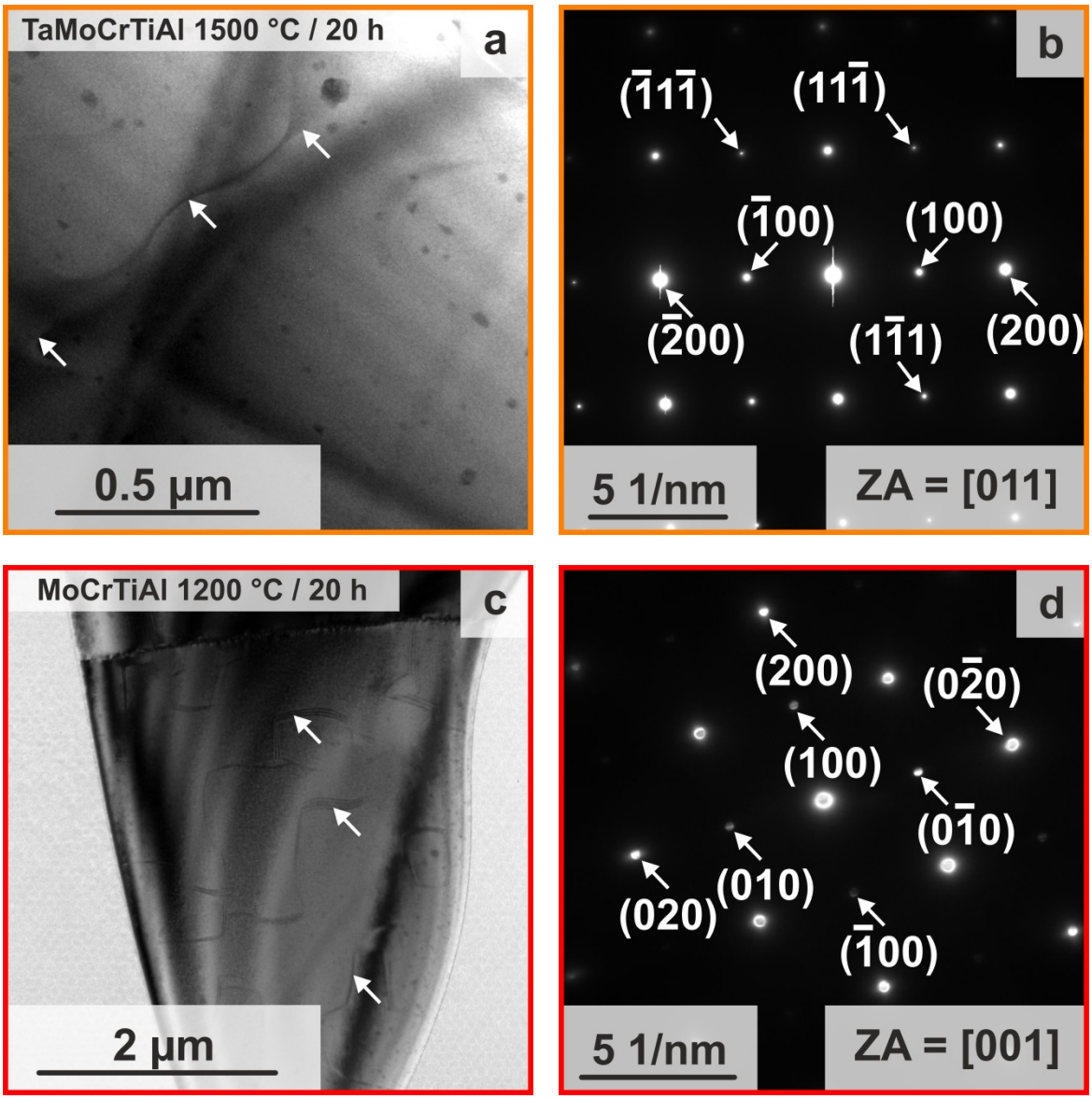

Figure 5: Overview of TEM investigations (TEM-BF images and corresponding TEM-SAD patterns) on: a) & b) TaMoCrTiAl c) &d) MoCrTiAl; arrows in a) and c) indicate planar defects; color code is identical to Figs. 1 & 4.

Since the observed ordering proceeds in the solid-state (as indicated by thermodynamic calculations), the planar defects could arise from thermal APDBs that form during cooling when the distinct domains

coalesce. The defects seem to be isotropic in the case of TaMoCrTiAl since their shape is curvy in the planar projection. On the other hand, the defects in MoCrTiAl reveal a certain anisotropy. The preferred crystallographic orientation of the planar defects in MoCrTiAl was further investigated by superlattice TEM-DF imaging to reveal the habit plane of these features (Fig. 6). When performing DF imaging using the diffraction vector $g = [\bar{1}00]$ (highlighted in the SAD pattern of Fig. 6a), the planar defects become visible as dark, mostly thin lines along $\langle 010 \rangle$ directions, as observed in Fig. 6b. Thus, it is concluded that the planar defects show characteristic contrast of an antiphase boundary with a {100} habit plane. Similar observations for anisotropic thermal APDBs with {100}-type habit planes were found for rapidly solidified B2-type TiPd alloys [19]. In the case of TiPd, the displacement vector was identified to be ½<111>. In contrast, the thermal APDBs of Fe-40Al-0.7C-0.5B with {100} habit planes reveal six variants of this planar defect with ½<100> displacement vectors [20]. Hence, the investigation of displacement vector for the planar defects in MoCrTiAl with {100} habit planes is of importance.

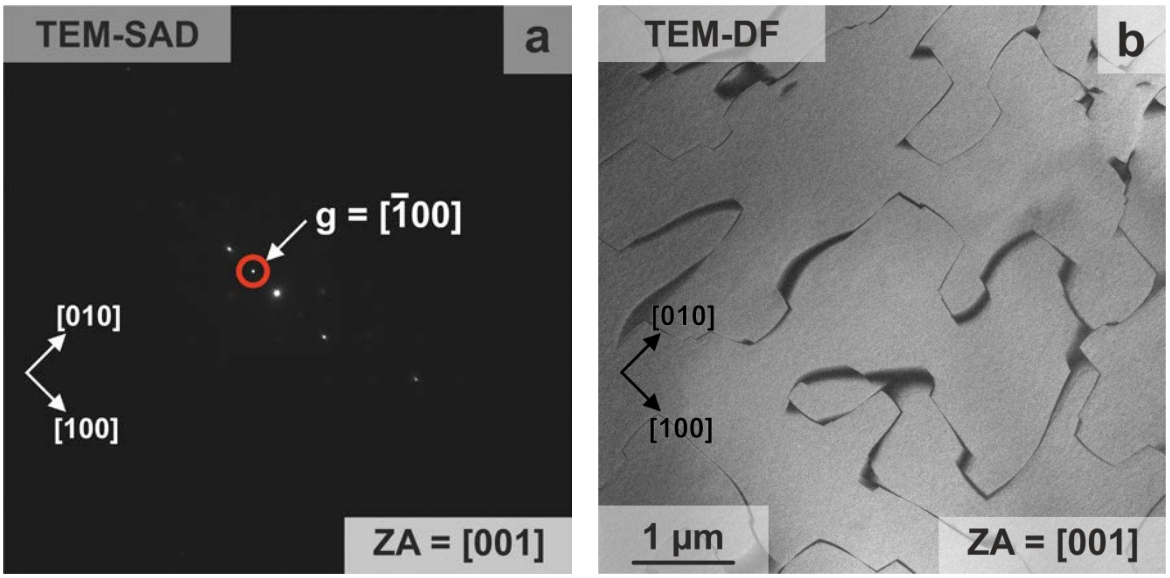

Figure 6: TEM-DF imaging on MoCrTiAl near zone axis ZA = [001]; a) Diffraction pattern shows diffraction vector $g = [\bar{1}00]$ for DF experiment and orientation of the SAD pattern; b) superlattice DF image acquired with $g = [\bar{1}00]$; SAD pattern and DF image have the same orientation.

The properties of the observed planar defects in MoCrTiAl were, therefore, examined at higher magnification. STEM-HAADF imaging at low magnification also reveals the presence of the planar defects and supports the observation of a {100} habit plane. Higher magnification of a region near such a feature (red square in Fig. 7a) provides evidence for a {100} habit plane, too (please see unit vectors in Fig. 7b). The fast Fourier transform (FFT) supports the TEM-SAD observations in Figs. 5b & d, revealing superlattice reflections of a B2-type superstructure (inset of Fig. 7b). An STEM-EDX line scan across the planar defect (along the arrow from Fig. 7b) shows Cr enrichment and Ti depletion at the

APDB, whereas Mo and Al concentrations do not vary significantly. Further chemical analysis of the planar defects was performed by APT. The tips from Fig. 2a were carefully examined regarding local fluctuation of the Cr content. Indeed, the presence of Cr segregation was revealed at a planar defect in the APT tip no. “IV” and is presented in Fig. 7d. As observed by STEM-EDX, enrichment in Cr and depletion in Ti at the APDB is also revealed by APT whereas Mo and Al are homogenously distributed. It is concluded that segregation of Cr and depletion of Ti at the planar defects occurs during furnace cooling from homogenization temperature. Again, similar observations have been made in boron-doped FeAl intermetallics [21]. The appearance of a boron-enriched segregation at {100} planar faults in FeAl40Ni3.8 with 400 ppm of B was confirmed by a combination of TEM and APT. The segregation layer thickness was ~3 nm [21] and is comparable to the thickness of the Cr-enriched and Ti-depleted layer in homogenized MoCrTiAl.

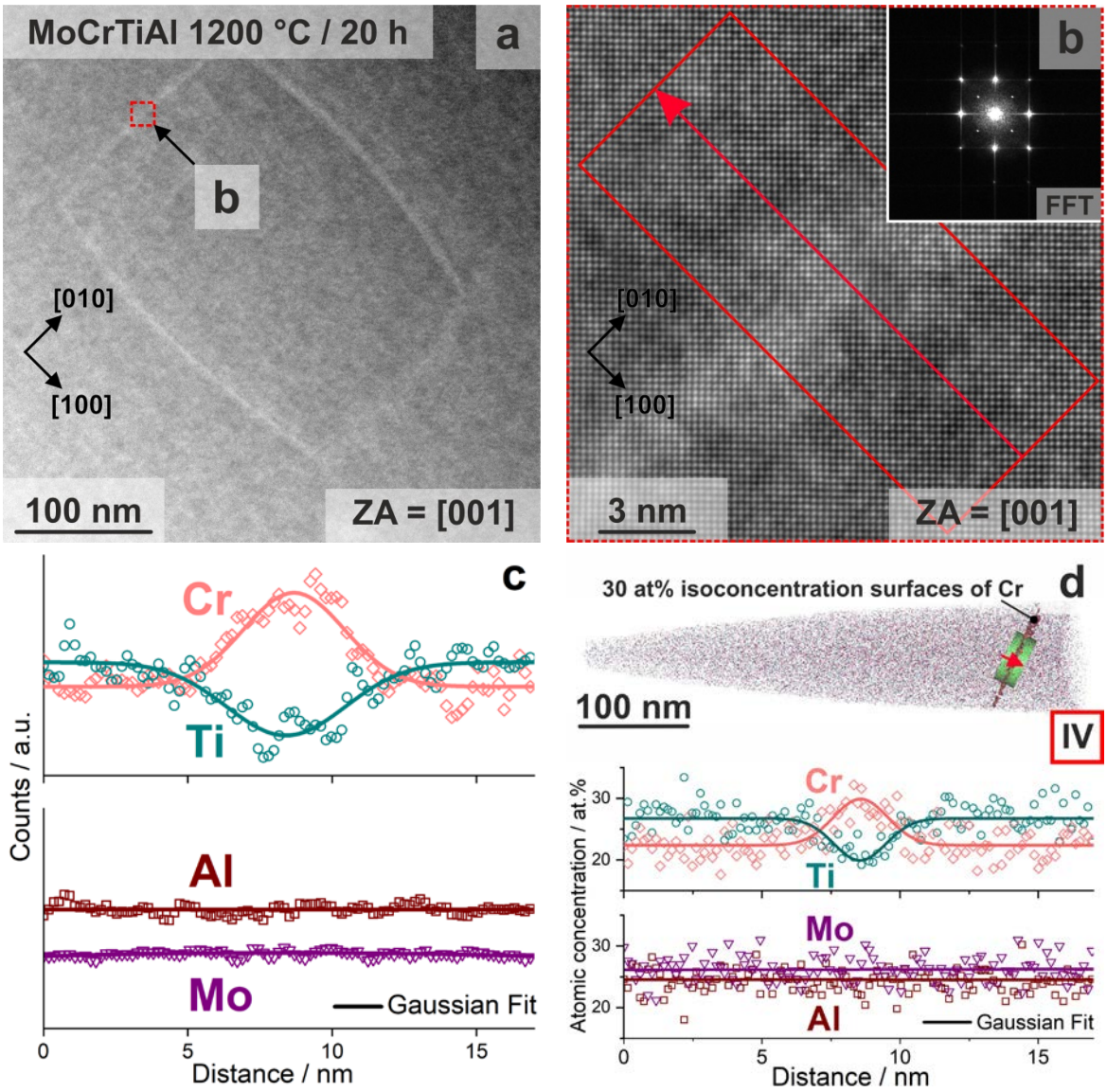

Figure 7: STEM-HAADF and APT investigations on planar defects in MoCrTiAl: a) STEM-HAADF image in [001] zone axis orientation at low magnification, b) High resolution STEM-HAADF image with the

corresponding FFT as inset, c) STEM-EDX line scan along the red arrow from b) with averaging in the region between the confining lines (symbols), d) APT investigations on APT tip no. “IV” containing an APDB: ion map including 30 at.% isoconcentration surfaces of Cr for identification of the planar defect and element concentration profile along red arrow of within the highlighted cylinder; color coding of the elements is identical to Figs. 1 &°2).

As already discussed, the observed planar defects of MoCrTiAl lie on {100}-type habit planes. However, STEM-HAADF imaging could not reveal the displacement vector of this defect since the atomic columns of the two distinct B2-lattice sites exhibit similar intensities. Hence, a virtual image shown in Fig. 8a was obtained from Fourier filtering the image of Fig. 7b by masking the B2-type superlattice reflections (inset of Fig. 8a). Qualitatively, regions with higher brightness exhibit a higher degree of order than faint regions. It should be noted that the region of segregation at the observed planar defect, which has a thickness of several atomic planes, appears to have a lower degree of order than the adjacent B2-regions. Within the B2-regions, slight fluctuations in the nearest neighbor atomic column intensity distributions and, hence, the extent of order is also detectable. When following the two lines, marked in Fig. 8a, the adjacent domains are displaced by $\frac{1}{2}[010]$ (the line lies on the bright columns in one domain and between the bright columns in the other one). Therefore, $\frac{1}{2}[010]$ is either the full displacement vector of this (100) plane or at least a projection of it. Consequently, both $\frac{1}{2}\langle 100\rangle$ such as in Fe-40Al-0.7C-0.5B [20] or $\frac{1}{2}\langle 111\rangle$ displacements as observed and Fe-37Al-15Mo [22] are conceivable. In both cases, chemical inhomogeneity is present at the planar defects and, thus, facilitate the observed habit plane and displacement vector. However, in the case of ½<111> displacement vectors, a chemical inhomogeneity must not be present, such as presented for TiPd [19]. More investigations on planar defects in MoCrTiAl with differently oriented habit planes are necessary to finally determine the displacement vector of this feature.

Fig. 8b presents a color map based on the nearest neighbor intensity distribution generated from the image shown in Fig. 7b. The color corresponds to the intensity difference of an atomic column and the mean intensity of its nearest neighboring columns. The intensity difference is zero if the lattice site occupation of neighboring atomic columns is equal and, therefore, the local arrangement can be considered to be random [23]. Intensity differences greater than zero indicate a certain extent of order. It should be mentioned that the absolute value of the intensity difference strongly depends on the TEM sample thickness and quality. Furthermore, there are at least two elements located in one B2-sublattice and, hence, in one atomic column (as already discussed in the context of the XRD measurements, Fig. 4). Thus, the low intensity difference indicates that the projected potential or the structure factor difference of the two sublattices is small; this supports the observed absence of B2-

reflections by XRD. However, the color map qualitatively reveals that the Cr-enriched and Ti-depleted layer at the planar defect appears to have a lower degree of order than the adjacent B2-type domains, as also observed by Fourier filtering (Fig. 8a). It is concluded that the B2-type domains could be wetted by a coherent secondary phase, which apparently is more of an A2-type. The formation of a Cr-enriched secondary phase is supported by STEM-EDX and APT of Figs. 7c & d. The formation of wetting layers with a lower degree of order at APDBs was found for B2-type ordered FeAl [24]. In this case, APDBs were wetted by a disordered Fe-rich phase of A2-type crystal structure.

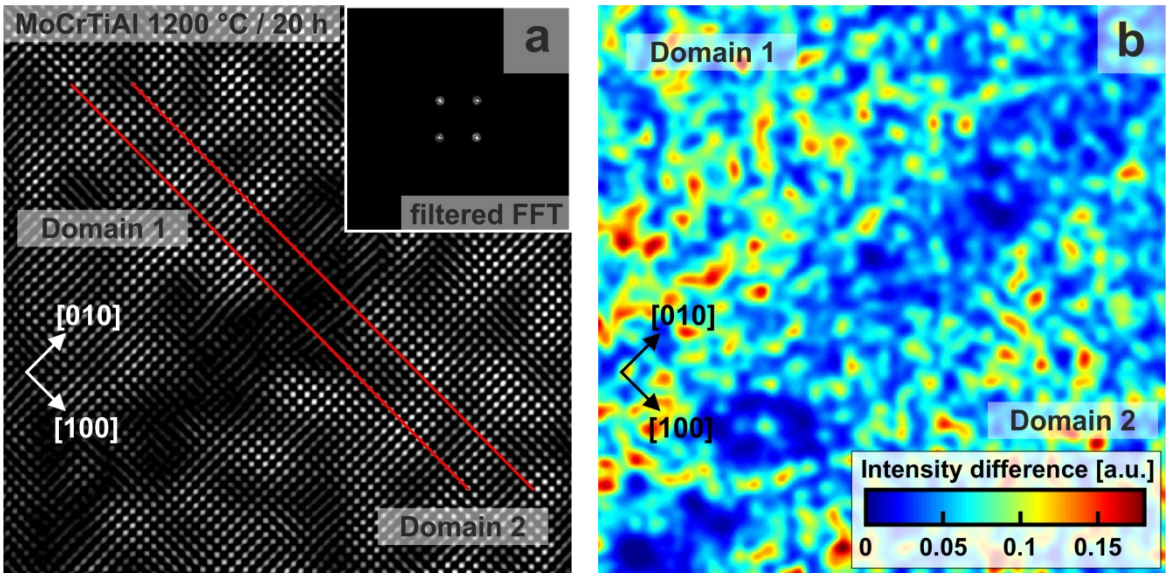

Figure 8: a) Superlattice Fourier filtered image using B2-type reflections (inset); aperture radius for masking the superlattice reflections was 10 pixels and the virtual apertures were smoothed by Gaussian filter, b) Intensity difference map of nearest neighbor atomic columns generated from the STEM-HAADF image of Fig. 7b.

3.3 Ordering transformation and segregation during furnace cooling

The ordering transformation as well as the formation of the planar defects and the segregation process might be detectable by thermal analysis. Hence, the temperature dependence of enthalpy dH/dT was determined by DSC and is presented in Fig. 9. To avoid possible additional signatures of precipitation of secondary phases (C14-type [6] and A15-type [5] phases), dH/dT was determined from the as-homogenized state (Tab. 1) of the alloys by DSC experiments on heating at a constant rate of 20 K/min within the temperature range of 300 °C up to 1450 °C. All alloys exhibit a λ-shaped peak at temperatures between $T_{\mathrm{peak}} = 990$ °C (1263 K, MoCrTiAl) and $T_{\mathrm{peak}} = 1264$ °C (1537 K, NbMoTiAl). Thus, the experimentally determined transition temperature of MoCrTiAl is 100 K lower than predicted by thermodynamic calculations (please compare with Fig. 3). In agreement with Ref. [25], the λ-shaped dH/dT indicates a second-order phase transformation which corresponds to the expected ordering transformation in the investigated alloys. In all investigated cases, an extended plateau region with an

enhanced dH/dT (colored temperature ranges in Fig. 9) is observed. The signature of a local maximum in MoCrTiAl, NbMoCrTiAl and NbMoTiAl in this temperature range is apparent (closed triangular symbols from Fig. 9) but was not found in TaMoCrTiAl. The onset temperatures of these features T_{onset} are observed between 569 °C (842 K, MoCrTiAl) and 797 °C (1070 K, NbMoTiAl). Below these onsets, dH/dT follows the expected trend given by the $c_p = 3 \cdot R$ limit of the heat capacity at high temperatures [26]. At the current state of research, the extended plateaus and local maxima (closed triangles) of dH/dT between T_{onset} and T_{peak} cannot be fully rationalized but it may be related to the segregation process at APDBs.

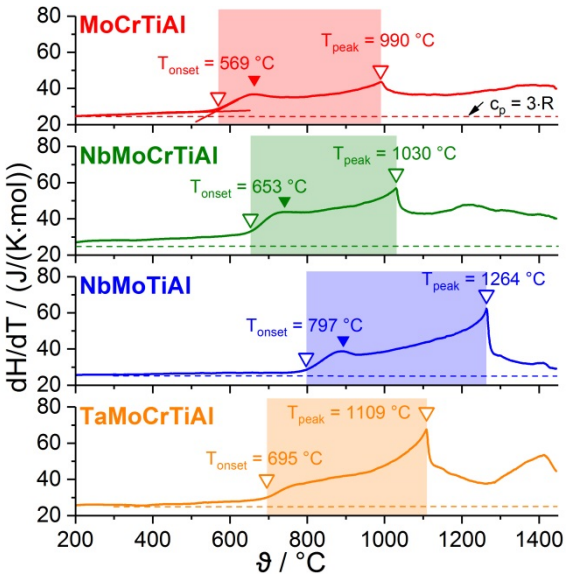

Figure 9: Overview of DSC experiments: temperature-dependent dH/dT of four alloys derived from the system Ta-Nb-Mo-Cr-Ti-Al; open triangles point out characteristic temperatures T_{peak} and T_{onset}; colored temperature range highlights extended plateau region of dH/dT; closed triangular symbols indicate local maxima in some of the alloys; dashed lines highlight $c_p = 3 \cdot R$ [26]; color code is identical to Figs. 1, 4 & 5.

4. Conclusions

We presented equiatomic alloys from the Ta-Nb-Mo-Cr-Ti-Al system which were arc-melted and subsequently homogenized at temperatures between 1200 °C up to 1500 °C. All microstructures were proven to be chemically homogenous in terms of SEM-BSE, SEM-EDX and APT. TEM-SAD patterns unambiguously reveal B2-type ordering (CsCl prototype) in all investigated alloys and, therefore, support predictions by thermodynamic calculations. It is concluded that the present B2-type ordering most probably contributes to the intrinsic brittleness of high entropy alloys derived from the Ta-Nb-Mo-Cr-Ti-Al system. The peculiarities of ordering were investigated in detail:

- The sample volume independent auto-correlation factor μ_i can be used for quantifying the chemical homogeneity in RHEAs. However, μ_i is not able to identify preferred crystallographic element site occupation in alloys with a large number of constituents because the investigated bins have a bin size that is much larger than the dimension of a single unit cell. Hence, crystallographic ordering which takes place on length scales of a Burger's vector cannot be revealed by this parameter. We suggest to carefully distinguish between "homogeneous" and "disordered".

- The absence of XRD superstructure peaks in multicomponent systems, such as the {100} peak of MoCrTiAl, is no unambiguous prove for disorder. It rather indicates that the structure factor ratio $\frac{|F_{\{100\}}|}{|F_{\{200\}}|}$ is small due to a counterbalancing of heavy and lighter elements on the different lattice sites according to the site occupation factors SOF_i^{LS}.

- Multiple species on a distinct Wyckoff position reduce the intensity difference between different atomic columns by Z-contrast, STEM-HAADF imaging. Thus, the elements site occupation cannot be revealed by this technique in multicomponent crystal superstructures.

- Planar defects with {100} habit planes in MoCrTiAl are wetted by a Cr-enriched and Ti-depleted segregation layer. Those planar defects form from former thermal APDBs. The wetting layer seems to have a lower extent of order and could give indications for further alloy development, regarding enhanced room temperature ductility by the stabilization of an entire A2 crystal structure in a non-equiatomic RHEA.

- DSC is able to detect the disorder-order phase transition temperatures precisely and reproducible since the signature of the altered heat capacity at the transformation temperature seems to be rather pronounced. This characterization method is independent of the specific site occupation and potential cancellation of scattering intensity in multi-component alloys. Crystallographic ordering can therefore be revealed or excluded rather than by X-ray diffraction experiments. In Ta-Nb-Mo-Cr-Ti-Al, the observed phase transitions are apparently of second-order. Both A2-type and B2-type phase occupy the same lattice and differ from each other only by the element site occupation. Hence, this type of transformation obviously can occur also up to very high cooling rates.

Acknowledgements

The financial support by the Deutsche Forschungsgemeinschaft (DFG), grant no. HE 1872/31-1, 34-1 and CL 2133/4-1 is gratefully acknowledged. AK thanks the Carl Zeiss Foundation for financial support

by a postdoc grant. The authors acknowledge the chemical analysis by ICP-OES at the Institute for Applied Materials (IAM-AWP), Karlsruhe Institute of Technology (KIT). K. Kaleta (Institute for Applied Materials (IAM-AWP), Karlsruhe Institute of Technology (KIT)) is appreciated for support in TEM sample preparation. We would like to thank S. Pasch, L. Wengenmayer, S. Laube, B.-D. Nguyen and F. Hinrichs for experimental support. This work was partly carried out with the support of the Karlsruhe Nano Micro Facility (KNMF, www.knmf.kit.edu), a Helmholtz Research Infrastructure at Karlsruhe Institute of Technology (KIT, www.kit.edu).

References

[1] J.-W. Yeh, S.-K. Chen, S.-J. Lin, J.-Y. Gan, T.-S. Chin, T.-T. Shun, C.-H. Tsau, S.-Y. Chang, Nanostructured High-Entropy Alloys with Multiple Principal Elements: Novel Alloy Design Concepts and Outcomes, Adv. Eng. Mater. 6 (2004) 299–303. doi:10.1002/adem.200300567.

[2] S. Gorsse, D.B. Miracle, O.N. Senkov, Mapping the world of complex concentrated alloys, Acta Materialia. 135 (2017) 177–187. doi:10.1016/j.actamat.2017.06.027.

[3] O.N. Senkov, G.B. Wilks, D.B. Miracle, C.P. Chuang, P.K. Liaw, Refractory high-entropy alloys, Intermetallics. 18 (2010) 1758–1765. doi:10.1016/j.intermet.2010.05.014.

[4] O.N. Senkov, D.B. Miracle, K.J. Chaput, J.-P. Couzinie, Development and exploration of refractory high entropy alloys—A review, J. Mater. Res. 33 (2018) 3092–3128. doi:10.1557/jmr.2018.153.

[5] H. Chen, A. Kauffmann, S. Laube, I.-C. Choi, R. Schwaiger, Y. Huang, K. Lichtenberg, F. Müller, B. Gorr, H.-J. Christ, M. Heilmaier, Contribution of Lattice Distortion to Solid Solution Strengthening in a Series of Refractory High Entropy Alloys, Metallurgical and Materials Transactions A. 49 (2018) 772–781. doi:10.1007/s11661-017-4386-1.

[6] H. Chen, A. Kauffmann, B. Gorr, D. Schliephake, C. Seemüller, J.N. Wagner, H.-J. Christ, M. Heilmaier, Microstructure and mechanical properties at elevated temperatures of a new Al-containing refractory high-entropy alloy Nb-Mo-Cr-Ti-Al, Journal of Alloys and Compounds. 661 (2016) 206–215. doi:10.1016/j.jallcom.2015.11.050.

[7] B. Gorr, F. Mueller, H.-J. Christ, T. Mueller, H. Chen, A. Kauffmann, M. Heilmaier, High temperature oxidation behavior of an equimolar refractory metal-based alloy 20Nb 20Mo 20Cr 20Ti 20Al with and without Si addition, Journal of Alloys and Compounds. 688 (2016) 468–477. doi:10.1016/j.jallcom.2016.07.219.

[8] O.N. Senkov, G.B. Wilks, J.M. Scott, D.B. Miracle, Mechanical properties of Nb25Mo25Ta25W25 and V20Nb20Mo20Ta20W20 refractory high entropy alloys, Intermetallics. 19 (2011) 698–706. doi:10.1016/j.intermet.2011.01.004.

[9] O.N. Senkov, S.V. Senkova, C. Woodward, Effect of aluminum on the microstructure and properties of two refractory high-entropy alloys, Acta Materialia. 68 (2014) 214–228. doi:10.1016/j.actamat.2014.01.029.

[10] O.N. Senkov, S.V. Senkova, D.B. Miracle, C. Woodward, Mechanical properties of low-density, refractory multi-principal element alloys of the Cr–Nb–Ti–V–Zr system, Materials Science and Engineering: A. 565 (2013) 51–62. doi:10.1016/j.msea.2012.12.018.

[11] D.X. Qiao, H. Jiang, X.X. Chang, Y.P. Lu, T.J. Li, Microstructure and Mechanical Properties of $VTaTiMoAl_x$ Refractory High Entropy Alloys, MSF. 898 (2017) 638–642. doi:10.4028/www.scientific.net/MSF.898.638.

[12] S. Chen, X. Yang, K. Dahmen, P. Liaw, Y. Zhang, Microstructures and Crackling Noise of AlxNbTiMoV High Entropy Alloys, Entropy. 16 (2014) 870–884. doi:10.3390/e16020870.

[13] M. Widom, W.P. Huhn, S. Maiti, W. Steurer, Hybrid Monte Carlo/Molecular Dynamics Simulation of a Refractory Metal High Entropy Alloy, Metall and Mat Trans A. 45 (2014) 196–200. doi:10.1007/s11661-013-2000-8.

[14] F. Körmann, M. Sluiter, Interplay between Lattice Distortions, Vibrations and Phase Stability in NbMoTaW High Entropy Alloys, Entropy. 18 (2016) 403. doi:10.3390/e18080403.
[15] N.D. Stepanov, D.G. Shaysultanov, G.A. Salishchev, M.A. Tikhonovsky, Structure and mechanical properties of a light-weight AlNbTiV high entropy alloy, Materials Letters. 142 (2015) 153–155. doi:10.1016/j.matlet.2014.11.162.
[16] N.Yu. Yurchenko, N.D. Stepanov, S.V. Zherebtsov, M.A. Tikhonovsky, G.A. Salishchev, Structure and mechanical properties of B2 ordered refractory AlNbTiVZr x (x = 0–1.5) high-entropy alloys, Materials Science and Engineering: A. 704 (2017) 82–90. doi:10.1016/j.msea.2017.08.019.
[17] M.P. Moody, L.T. Stephenson, A.V. Ceguerra, S.P. Ringer, Quantitative binomial distribution analyses of nanoscale like-solute atom clustering and segregation in atom probe tomography data, Microscopy Research and Technique. 71 (2008) 542–550. doi:10.1002/jemt.20582.
[18] M.J. Yao, K.G. Pradeep, C.C. Tasan, D. Raabe, A novel, single phase, non-equiatomic FeMnNiCoCr high-entropy alloy with exceptional phase stability and tensile ductility, Scripta Materialia. 72–73 (2014) 5–8. doi:10.1016/j.scriptamat.2013.09.030.
[19] T. Hara, E. Okunishi, M. Nishida, M. Matsuda, High-angle annular dark field scanning transmission electron microscopy of the antiphase boundary in a rapidly solidified B2 type TiPd compound, Philosophical Magazine Letters. 87 (2007) 59–64. doi:10.1080/09500830601105667.
[20] L. Pang, M.F. Chisholm, K.S. Kumar, {001} faults in B2 Fe-40 at.% Al-0.7 at.% C-0.5 at.% B, Philosophical Magazine Letters. 78 (1998) 349–355. doi:10.1080/095008398177742.
[21] E. Cadel, A. Fraczkiewicz, D. Blavette, Suzuki effect on {001} stacking faults in boron-doped FeAl intermetallics, Scripta Materialia. 51 (2004) 437–441. doi:10.1016/j.scriptamat.2004.04.026.
[22] U. Prakash, R.A. Buckley, H. Jones, Novel faulted structures in rapidly solidified Fe-37 at.% Al-15 at.% Mo alloy, Acta Metallurgica et Materialia. 39 (1991) 1677–1682. doi:10.1016/0956-7151(91)90256-Z.
[23] C.H. Liebscher, M. Yao, P. Dey, M. Lipińska-Chwalek, B. Berkels, B. Gault, T. Hickel, M. Herbig, J. Mayer, J. Neugebauer, D. Raabe, G. Dehm, C. Scheu, Tetragonal fcc-Fe induced by κ -carbide precipitates: Atomic scale insights from correlative electron microscopy, atom probe tomography, and density functional theory, Physical Review Materials. 2 (2018). doi:10.1103/PhysRevMaterials.2.023804.
[24] J.E. Krzanowski, S.M. Allen, The migration kinetics of antiphase boundaries wetted by a second phase, Acta Metallurgica. 31 (1983) 213–222. doi:10.1016/0001-6160(83)90081-0.
[25] R. Santamarta, E. Cesari, J. Font, J. Muntasell, J. Pons, J. Dutkiewicz, Effect of atomic order on the martensitic transformation of Ni–Fe–Ga alloys, Scripta Materialia. 54 (2006) 1985–1989. doi:10.1016/j.scriptamat.2006.03.018.
[26] P.L. Dulong, A.-T. Petit, Recherches sur quelques points importans de la theorie de la Chaleur, Annales de Chimie et de Physique. 10 (1819) 395–413.